ORIGINAL PAPER

A discrete element framework for modeling the mechanical behaviour of snow Part II: model validation

Bernhard Peters[1] · B. Wendlassida Kabore[1] · Mark Michael[1] · Francois Nicot[2]

Abstract

A micro-scale modelling approach of snow based on the extension of the classical discrete element method has been presented in the first part of this study. This modelling approach is employed to predict the mechanical response of snow under compression dependent on strain rate, initial density and temperature. Results obtained under a variety of conditions are validated with experimental data for both micro- and macro-scale, in particular the broad range between ductile i.e. low deformation rates and brittle i.e. high deformation rates regimes are investigated. For this purpose snow is assumed to be composed of ice grains that are inter-connected by a network of bonds between neighbouring grains. This arrangement represents the micro-scale of which the interaction is described by inter-granular collision and bonding. Hence, the response on a macro-scale is largely determined by inter-granular collisions and deformation and failure of bonds during a loading cycle. Consequently, validation was first carried out on micro-scale deformations at different loading rates and temperatures. Hereafter, macro-scale simulations of confined and unconfined, deformation-controlled compression tests have been predicted and were successfully compared to experimental data reported in literature.

1 Introduction

The first part of this contribution proposed an extended discrete element method as developed by Peters et al. [23] that describes the mechanical behavior of snow on both a micro- and macro-scale under various loading conditions. Within this approach snow is considered to consist of individual ice grains that are inter-connected by a network of binds to from a porous structure. Models developed for grain collisions, bond generation, deformation and fracture describe the inter-granular forces and moments for a loaded snow pack under a variety of conditions such as pressure, temperature and loading rates. The modelling approach, thus, describes the characteristics for a micro-structure e.g. grain scale and includes elastic-plastic grain collision, inter-granular friction, bond

growth due to creep of ice, elastic viscous-plastic deformation and fracture of bonds. The algorithms employed are based on the ice-ice sintering measurements of [26], on the contact theory of [14] and on creep models of ice developed by [3]. A similar approach based on discrete element modelling was employed by Hagenmuller et al. [12]. They represented the snow matrix by sphere clumps representing a grain that are interconnected by cohesion forces. A simple linear spring model was applied to evaluate the normal force between grains. If the normal force exceeds a given threshold the normal force is neglected meaning that cohesion is broken. Similarly, a shear force acting in the tangential plane between two grains was introduced whereby the cohesive strength in normal and tangential direction were defined by the same value. They concluded from a comparison between experimetal data and predictions of a confined compression test, that snow density is dominant for the mechanical behavior. Kabore et al. [15–17] employed linear viscoelastic Euler-Bernoulli beams to represent cohesive forces and torques between sintered particles through bending, twisting and stretching of the beams. The model was validated with snow compression data obtained from the literature. Their study

✉ B. Wendlassida Kabore
  brice.wendlassida@gmail.com

1   FSTC, Université du Luxembourg, 6 rue
    Coudenhove-Kalergi, L-1359 Luxembourg, Luxembourg

2   IRSTEA, Université Grenoble-Alpes,
    F38402 Saint Martin d'Hères Cedex, France

focused on short-term behavior and did not include long-term creep and plasticity for higher contact stresses. Gaume et al. [9, 11] investigated crack propagation in weak snow pack layers with a discrete element approach. For this purpose, two horizontal slabs of snow represented by discrete elements were connected by beam-like discrete elements. Normal contact was described by a linear-spring dashpot model and the tangential contact model included a linear part combined with Coloumb friction. The cohesive part of the contact model was composed of a linear behavior in both normal and tangential direction. The cohesive bonding in both directions was assumed to break if a given tensile strength and shear stress is exceeded and thus, represents a weak layer. Cracks are expected to propagate and trigger an avalanche [5, 8, 10, 13]. Findings of Gaume et al. [9, 11] indicate that the crack propagation speed increases with an increasing young's modulus and weight of the slabs. However, more research into the structural bahaviour of snow is required as stated by Gaume et al. [9, 11] and is addressed in the current study.

The objective of the second part is to validate the proposed modelling framework on both a grain scale representing the micro-mechanical behavior and a macro- scale for compression tests of snow samples. In particular a variety of loading rates designating the ductile and brittle regime of snow at different temperatures was emphasised and compared with experimental data.

2 Numerical model

This section is an extract of part I to summarise the main equations of the modelling approach. It allows linking the modelling techniques with the validation of the experimental data employed. For more details on the numerical model, the reader is referred to part I.

2.1 Mechanical properties

Elasticity of ice: Ice has an elastic-plastic behaviour that additionally is dependent on temperature as reported by [7]. They approximated elastic parameters by a linear relationship of the following form:

$$X(T) = X(T_0)[1 + 1.42 \cdot 10^{-3} \mathrm{K}^{-1} \cdot (T - T_0)] \tag{1}$$

where X stands for the Young's and shear modulus according to [7] and is commonly valid between $-16°\mathrm{C}$ and $-3°\mathrm{C}$. In the present work, we assume that this relation is valid for temperatures ranging between $-23°\mathrm{C}$ and $-1°\mathrm{C}$. The Young's and shear modulus are defined at a reference temperature of $T_0 = 243.15\ K$ as $E = 9.33$ GPa and $G = 3.45$

GPa, respectively. Poisson's Ratio is derived from the Young's and shear modulus as $v = E/2G - 1$.

Creep rate of ice:

$$\dot{\varepsilon}_\mathrm{I} = A \cdot \sigma^\mathrm{n} \cdot e^{\frac{-Q}{RT}} \tag{2}$$

$$\dot{\varepsilon}_\mathrm{II} = A' \cdot (\sinh(\alpha \cdot \sigma))^\mathrm{n} \cdot e^{\frac{-Q}{RT}} \tag{3}$$

where σ is the stress, R the gas constant, Q the activation energy, T the temperature and n, A and A' are model constants.

Hardness of ice:

$$H^* = B \cdot \left(\frac{1}{t}\right)^{\frac{1}{m}} \cdot e^{\frac{Q}{mRT}} \tag{4}$$

where Q, R and T denote activation energy, gas constant, temperature, respectively, and m and B are constants taken from [3]. t stands for the indentation time.

Friction Coefficient of Ice:

$$\mu_\mathrm{ice}(v_\mathrm{c}, T_\mathrm{c}, p_\mathrm{c}, H_\mathrm{c}) = C_\mu(T_\mathrm{c} - T_a)^\mathrm{a} \cdot p_\mathrm{c}^{-\mathrm{b}} \cdot \left(\frac{k\rho c_\mathrm{p}}{v_\mathrm{c} L}\right)^\mathrm{c} \cdot H_\mathrm{c}^{-\mathrm{d}} \tag{5}$$

where C_μ, T_a, k, ρ, c_p and L denote a constant nominally equal to 1.88, temperature of the contact partner, thermodynamic properties i.e. conductivity, density, heat capacity and characteristic length of the sliding body. The exponents usually take values of $a = 1$, $b = 0.25$, $c = 0.5$ and $d = 0.75$ according to [2].

Energy dissipation during collision: In the quasi-elastic regime of $v_\mathrm{i} < 0.4\ \mathrm{ms}^{-1}$, the coefficient of restitution remains constant with varying velocity and the potential energy is almost completely recovered after collision. In the regime of $v_\mathrm{i} > 0.4\ \mathrm{ms}^{-1}$ ice grains deform at impact and even break for very large impact velocities so that the coefficient of restitution deceases with increasing impact velocity.

$$e_\mathrm{ice} = \begin{cases} \cong 1 & v_\mathrm{i} < v_\mathrm{c} \\ \left(\frac{v_\mathrm{i}}{v_\mathrm{c}}\right)^{-\log\frac{v_\mathrm{i}}{v_\mathrm{c}}} & v_\mathrm{i} \geq v_\mathrm{c} \end{cases} \tag{6}$$

The above equation allow to account for energy dissipation du to grain damage and plasticity in high impact collisions i.e. for a relative velocity above the critical value v_c.

2.2 Modelling technique

The following model characteristics are taken into account:

- creep behaviour of ice
- temperature T and contact pressure p
- elastic-viscous-plastic deformation

- bond growth
- material properties of ice
- bond fracture
- pressure melting of contacting grains

Inter-granular forces and moments: Forces comprise all contact forces due to collision $\vec{F}_i^c$, bonding $\vec{F}_i^b$, gravitation $\vec{F}_i^g$ and external forces $\vec{F}_i^e$ as follows:

$$\vec{F}_i = \vec{F}_i^c + \vec{F}_i^b + \vec{F}_i^g + \vec{F}_i^e \qquad (7)$$

Collision Forces: The normal force for a collision writes as

$$\vec{F}_{ij}^{c,n} = \vec{n}_{ij} \cdot \begin{cases} -k_1^n \cdot \delta_{ij}^{n,e} & : \dot{\delta}_{ij}^n \geq 0 \\ -k_{unl}^n \cdot (\delta_{ij}^{n,e} - \delta_{ij}^{n,p}) & : \dot{\delta}_{ij}^n < 0 \wedge \delta_{ij}^n \geq \delta_{ij}^{n,p} \end{cases} \qquad (8)$$

where k_1^n, k_{unl}^n and $\dot{\delta}_{ij}^n$ denote loading, unloading stiffness and overlap rate, respectively, while the tangential component is defined through

$$\vec{F}_{ij}^{c,t} = -\vec{t}_{ij} \cdot \min\left(|c_t \dot{t}|, \mu_{ice} \cdot |\vec{F}_{ij}^{c,n}| \right) \qquad (9)$$

where $\vec{t}_{ij}$, c_t, $\dot{t}$ and $\vec{F}_{ij}^{c,n}$ denote the tangential direction, tangential damping coefficient, relative tangential velocity and normal collision force, respectively.

Bond forces: The total strain $\vec{\varepsilon}_{tot}$ is composed of an elastic strain ε_e and a viscous-plastic strain ε_{vp} as follows:

$$\vec{\varepsilon}_{tot} = \vec{\varepsilon}_e + \vec{\varepsilon}_{vp} \qquad (10)$$

with the total strain components as

$$\vec{\varepsilon}_{ij} = \begin{pmatrix} \varepsilon_{ij}^n \\ \varepsilon_{ij}^t \\ \gamma_{ij}^n \\ \gamma_{ij}^b \end{pmatrix} = \frac{1}{L_b} \cdot \begin{pmatrix} \Delta u_{ij}^n \\ \Delta u_{ij}^t \\ \Delta \phi_{ij}^n \cdot r_b \\ \Delta \phi_{ij}^b \cdot r_b \end{pmatrix} = \Delta t \cdot \frac{1}{L_b} \cdot \begin{pmatrix} \vec{v}_{ij} \cdot \vec{n}_{ij} \\ \vec{v}_{ij} \cdot \vec{t}_{ij} \\ \vec{\omega}_{ij} \cdot \vec{n}_{ij \cdot r_b} \\ \vec{\omega}_{ij} \cdot \vec{b}_{ij \cdot r_b} \end{pmatrix} \qquad (11)$$

that yields the elastic strain components

$$\vec{\varepsilon}_{ij}^e = \begin{pmatrix} \varepsilon_{ij}^{n,e}(t) \\ \varepsilon_{ij}^{t,e}(t) \\ \gamma_{ij}^{n,e}(t) \\ \gamma_{ij}^{b,e}(t) \end{pmatrix} = \sum_{i=1}^{i_b} \begin{pmatrix} \varepsilon_{ij}^n(t) - \dot{\varepsilon}_{ind}\left(\sigma_{ij}^n(t-\Delta t), T\right) \cdot \Delta t \\ \varepsilon_{ij}^t(t) - \dot{\varepsilon}_{ind}\left(\sigma_{ij}^t(t-\Delta t), T\right) \cdot \Delta t \\ \gamma_{ij}^n(t) - \dot{\varepsilon}_{ind}\left(\tau_{ij}^n(t-\Delta t), T\right) \cdot \Delta t \\ \gamma_{ij}^b(t) - \dot{\varepsilon}_{ind}\left(\tau_{ij}^b(t-\Delta t), T\right) \cdot \Delta t \end{pmatrix} \qquad (12)$$

The stress components are derived from the strain components and may be arranged in a column vector as follows:

$$\vec{\sigma}_{ij} = \begin{pmatrix} \sigma_{ij}^n \\ \sigma_{ij}^t \\ \tau_{ij}^n \\ \tau_{ij}^b \end{pmatrix} = \frac{E}{(1+v) \cdot (1-2v)} \begin{pmatrix} (1-v) \cdot \varepsilon_{ij}^{n,e} \\ 2 \cdot (1-2v) \cdot \varepsilon_{ij}^{t,e} \\ (1-2v) \cdot \gamma_{ij}^{n,e} \\ \frac{(1+v)}{(1-2v)^{-1}} \cdot \gamma_{ij}^{b,e} \end{pmatrix} \qquad (13)$$

where σ_{ij}^n, σ_{ij}^t, τ_{ij}^n and τ_{ij}^b stand for the stress developing under tension or compression, shear induced stress component, stress component created by torsion and bending of a bond, respectively. The Young's modulus E and the Poisson's ratio $v = E/G - 1$ are temperature dependent and are taken from eq. 1 according to [7].

Bond forces $\vec{F}_{ij}^{b,n}$ in normal direction and $\vec{F}_{ij}^{b,t}$ in tangential direction are obtained by multiplying the normal and tangential stress component by the bond area. Hence, multiplying the normal stress component σ_{ij}^n with the current bond area $A_{ij}^b(t)$ gives the normal bond force $\vec{F}_{ij}^{b,n}$ as

$$\vec{F}_{ij}^{b,n} = \sigma_{ij}^n \cdot \vec{n}_{ij} \cdot A_{ij}^b(t) \qquad (14)$$

and is acting along the normal direction due to tension and compression of a bond. Similarly, the tangential bond force $\vec{F}_{ij}^{b,t}$ results from the shear stress σ_{ij}^t as

$$\vec{F}_{ij}^{b,t} = \sigma_{ij}^t \cdot \vec{t}_{ij} \cdot A_{ij}^b(t) \qquad (15)$$

The current bond area $A_{ij}^b(t) = f\left(\sigma_{ij}^n(t-\Delta t), T\right)$ depends on the previous normal stress $\sigma_{ij}^n(t-\Delta t)$ and the ambient temperature T based on the sintering model of ice grains by [26]:

$$A_{ij}^b(t) = \pi \cdot \left\{ R_{ij}^2 - \left[\sqrt{R_{ij}^2 - r_{ij}^b(t-\Delta t)^2} \right. \right. \\ \left. \left. - \dot{\varepsilon}_{ind}\left(\sigma_{ij}^n(t-\Delta t), T\right) \cdot L_b \cdot \Delta t \right]^2 \right\} \qquad (16)$$

where R_{ij}, $r_{ij}^b(t-\Delta t)$, $\dot{\varepsilon}_{ind}$ and L_b denote the effective radius, previous bond radius, creep rate and bond length, respectively.

3 Macroscopic behaviour of snow

The current section addresses the macroscopic scale including relevant predicted results that are compared to measurements. Accordingly, the obtained results cover brittle, transitional and ductile behavior for unconfined and confined compression tests.

Compression tests of simple sample geometries such as cylindrical ones are the most common characteristic set-ups to study the mechanical behavior of snow. Hence, unconfined and confined compression tests in conjunction with a deformation controlled load plate under different loading rates $\dot{\varepsilon}_l$ and the temperatures T are preferred within this

Table 1 Temperatures and compression rates during compression tests

$T\,[^oC]$	−1	−4	−10	−16	−32	
$\dot{\epsilon}_l\,[s^{-1}]$	4	0.4	0.04	$4 \cdot 10^{-3}$	$4 \cdot 10^{-4}$	$4 \cdot 10^{-6}$

Table 2 Initial dimensions and densities of snow samples for prediction of compression tests

Sample	$\rho_0[kg/m^3\,]$	$2 \cdot r_c[mm]$	$h_c[mm]$	N_g
1	408 ±0.7%	58.0	86.0	1700
2	509 ±0.6%	2.9	3.92	1700
3	509 ±0.7%	5.8	8.4	13950
4	509 ±0.7%	116.1	167.3	13950
5	511 ±0.8%	58.0	74.4	1700
6	580 ±0.7%	5.8	7.4	13950
7	580 ±0.7%	116.1	147.4	13950

framework. Furthermore, parameters studied during tests include snow density ρ_0, grain size r_g and distribution, coordination number N_b of the bonds and initial bond strength r_b, i.e. size. The predictions of the unconfined compression tests follow the experimental setup of [18, 28] and [25], while rigid-confined compression tests are carried out according to the conditions chosen by [1, 6, 29] and [30]. The response of a snow sample during compression was studied at different temperatures and strain rates which are listed in table 1.

3.1 Snow sample preparation

Cylindrical snow samples of three different initial densities, $\rho_0 \sim 400$ kg/m^3, $\rho_0 \sim 500$ kg/m^3 and $\rho_0 \sim 600$ kg/m^3 have been prepared by the gravitational deposition method. The grain size distribution follows a linear distribution function $D(r_g)$ that writes as follows:

$$r_g = r_{min} + \left(r_{max} - r_{min}\right) \cdot \widetilde{x} \tag{17}$$

where r_g describes the grain radius and $r_{min} = 2.356$mm and $r_{max} = 2.604$ are the minimum and maximum grain radii, respectively. $\widetilde{x}$ is computed by a random generator $\widetilde{x} = random(0...1)$. The linear size distribution correlates well with sieves curves of snow. The grain size distribution results in a mean radius of $\overline{r}_g = 2.48$ mm and was employed for the current samples. Table 2 summarises the initial dimensions and properties of the prepared snow samples with their initial radius r_c, initial sample height h_c and number of grains N_g.

Figures 1 and 2 depict the arrangements of grains in a sample with their associated network of bonds for samples 1,5 and 7.

The density distributions of the samples as a centre slice are shown in Fig. 3. These density distributions are derived from a Voronoi tessellation proposed by [24] and illustrate an increasing density field with increasing initial density.

In addition, the initial bond strength and coordination number are subject to investigations for the chosen samples whereby the ratio $r_b/\overline{r}_g$ between bond and grain radius is employed to determine the initial bond size. The average number of bonds per grain N_b of a snow sample writes as follows:

$$N_b = \frac{1}{N_g} \cdot \sum_{i=1}^{N_g} N_i^b \tag{18}$$

where N_i^b and N_g refer to the number of bonds per grain i and number of grains, respectively. Thus, the following

Fig. 1 Arrangement of grains for three cylindrical snow samples

(a) Sample 1
$\rho_0 \approx 408\%$kg/m^3.

(b) Sample 5
$\rho_0 \approx 511\%$kg/m^3.
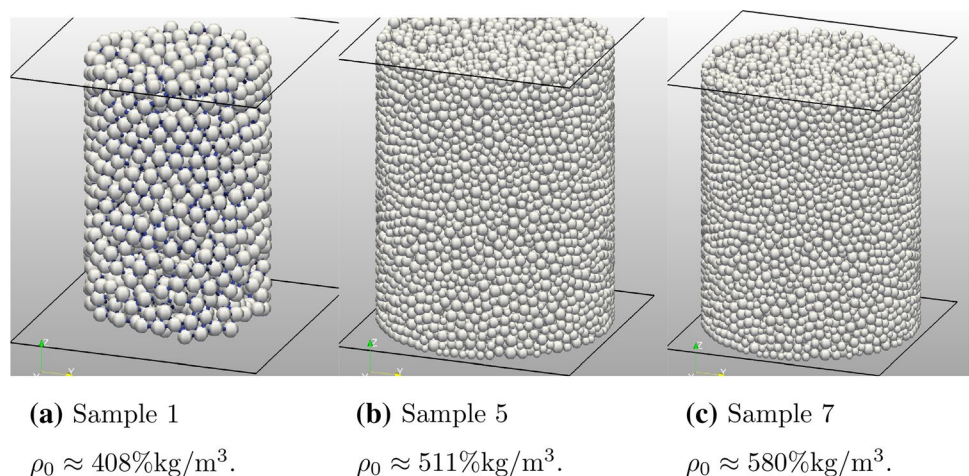
(c) Sample 7
$\rho_0 \approx 580\%$kg/m^3.

coordination numbers are estimated dependent on the ratio $r_b/\bar{r}_g$ and are listed in Table 3.

Furthermore, Table 3 highligts the additional dependency of number of bonds per grain N_b on the sample density. Although samples 5 and 6 have the same ratio $r_b/\bar{r}_g$, their coordination numbers are different due to different densities. The higher density of sample 6 as compard to sample 5 increases the coordination number and vice versa.

3.2 Unconfined compression tests of snow

Predictions carried out for different strain rates cover brittle, ductile, and associated transitional behavior between ductile and brittle regimes. Distinguishing the mechanical behavior of snow by the strain rate is a well established convention within the research field as stated by [18, 22] and [6]. The experimental results of [18] and [6] suggest a transition between brittle and ductile behavior at a strain rate of $\dot{\varepsilon} \sim 5 \cdot 10^{-4}\,\mathrm{s}^{-1}$.

(a) Sample 1: $\frac{r_b}{\bar{r}_g} = 0.5$, $N_b = 3$

(b) Sample 5: $\frac{r_b}{\bar{r}_g} = 0.5$, $N_b = 3.5$

(c) Sample 7: $\frac{r_b}{\bar{r}_g} = 0.1$, $N_b = 3$
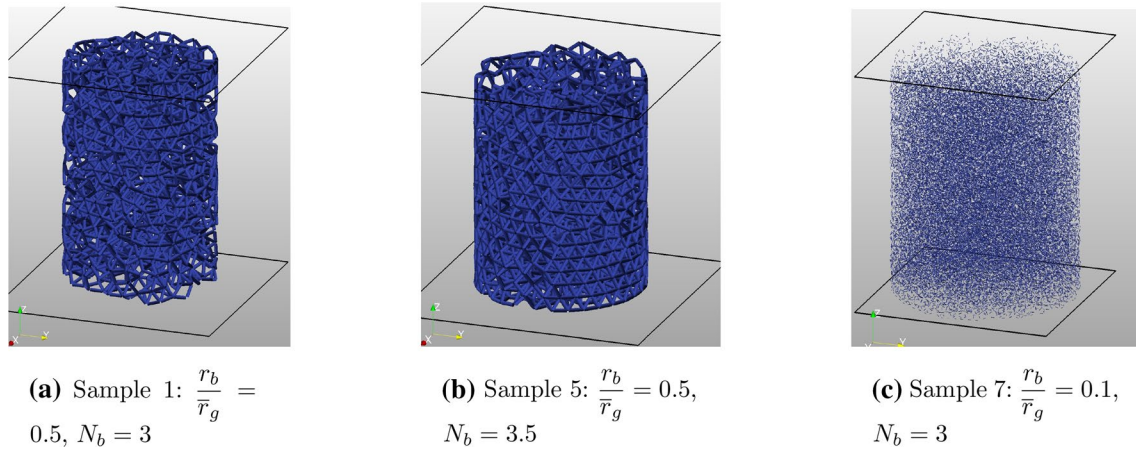
Fig. 2 Network of inter-connecting bonds for three cylindrical snow samples

(a) Sample 1: $\rho_0 \sim 408$ kg/m^3

(b) Sample 5: $\rho_0 \sim 511$ kg/m^3

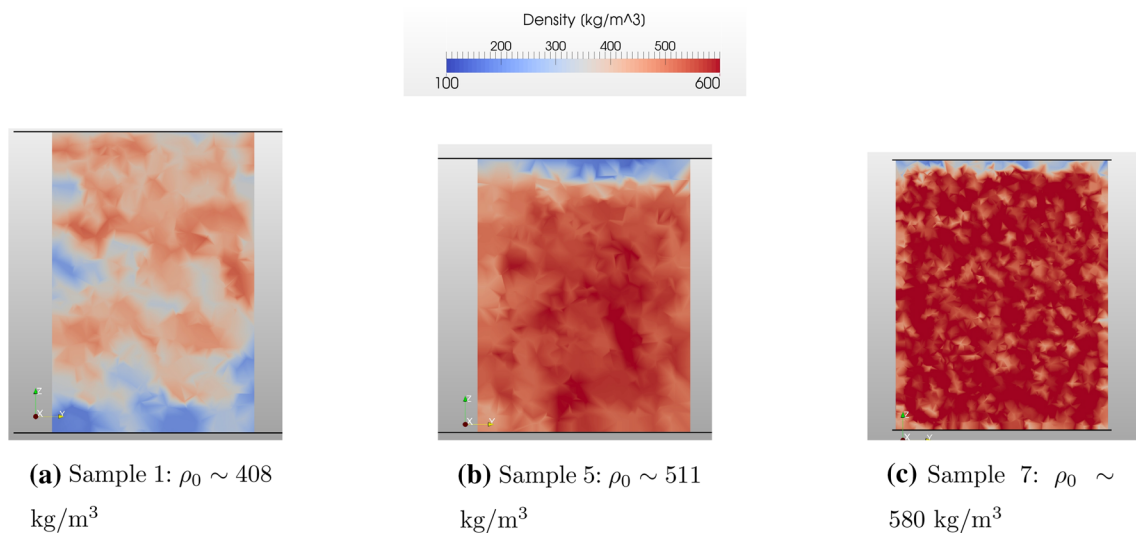**(c)** Sample 7: $\rho_0 \sim 580$ kg/m^3

Fig. 3 Density distribution in a slice for three snow samples

Table 3 Coordination number depending on the ratio of bond to grain radius

$r_b/\bar{r}_g$	0.1	0.3	0.3	0.3	0.5	0.5	0.9
N_b	1.0	2.5	3.0	3.5	3.0	3.5	4.0
Density [kg/m^3]	408	509	509	509	511	580	580

3.2.1 Deformation behaviour in the brittle regime

The response of snow samples with an initial density of $\rho_0 \sim 408$ kg/m^3 subjected to two strain rates of $\dot{\varepsilon} = 4 \cdot 10^{-2}$ s^{-1} and $\dot{\varepsilon} = 4 \cdot 10^{-3}$ s^{-1} well above the transitional strain rate at a temperature of $T = -2°$C have been predicted and are compared to experimental data of [18] as depicted in Fig. 4.

The profiles of Fig. 4 take the characteristic saw-tooth shape of the brittle deformation regime. After an almost initial linear increase of stress with strain an abrupt decrease in stress with almost no plastic deformation takes place. With increased strain the stress increases again with almost the

same gradient as previously. When the stress reaches a maximum value, the stress collapses again and hereafter follows repeating cycles, also observed by [6]. The maximum stress reached over the repeated ruptures is defined as the strength or yield stress σ_y of the brittle deformed sample. This cyclic behavior is caused by a surface fracture close to the bottom end of the snow sample as shown in Figs. 5 and 6 corresponding to a strain rate of $\dot{\varepsilon} = 4 \cdot 10^{-2}$ s^{-1}.

[18] described this type of brittle fracture as a non-uniform contraction with break downs concentrated at the top or bottom of the sample as occurring around the bottom part in Fig. 5. Fractures propagate into the sample into the lower

Fig. 4 Unconfined compression of a cylindrical snow sample in the brittle regime. The green lines are the predicted results at different brittle rates with an initial density of $\rho = 408$ kg/m^3. The black curve is a unconfined compression test of [18] at the brittle rate of about 10^{-3} s^{-1} (colour figure online)

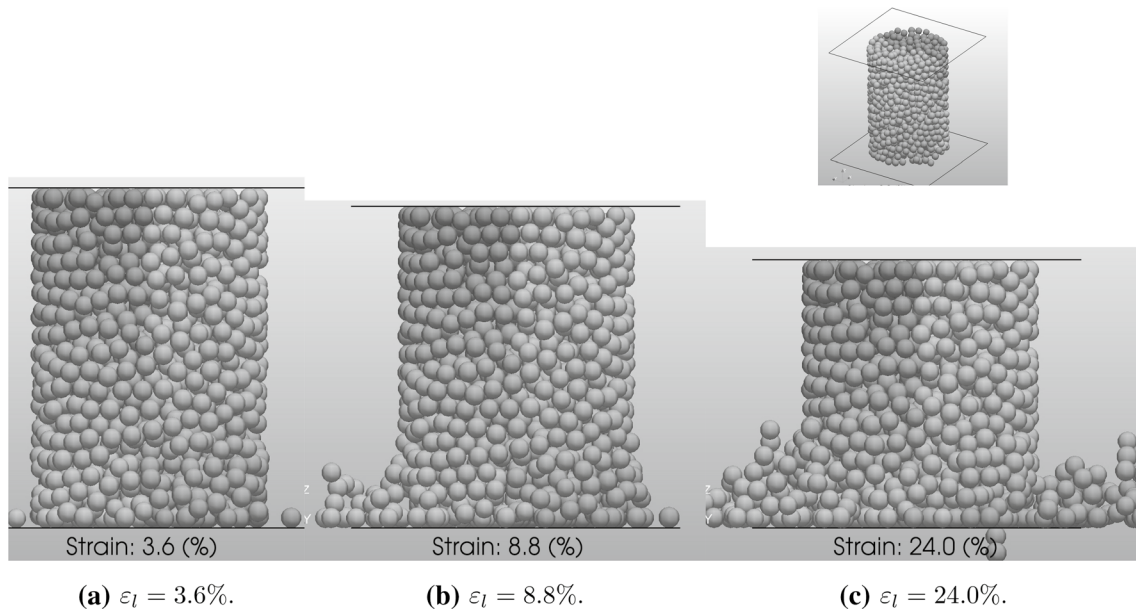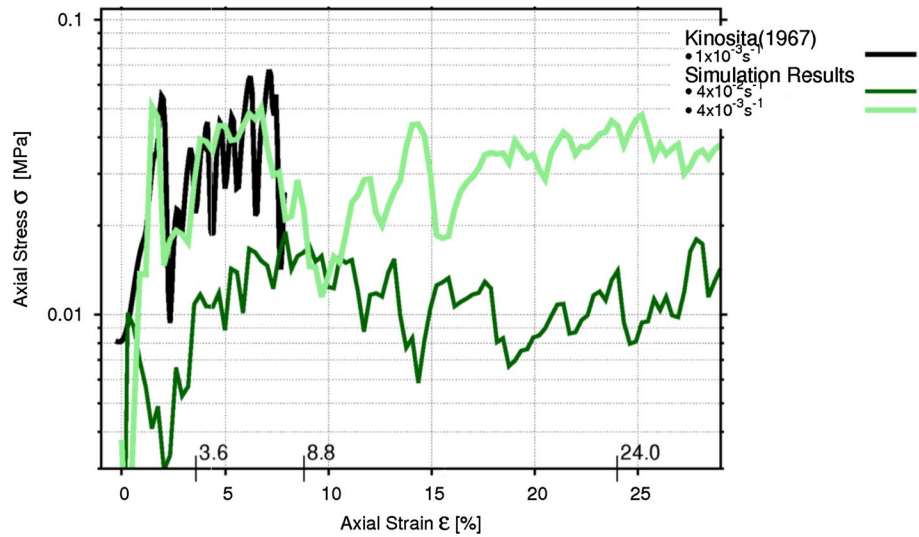**(a)** $\varepsilon_l = 3.6\%$.   **(b)** $\varepsilon_l = 8.8\%$.   **(c)** $\varepsilon_l = 24.0\%$.

Fig. 5 Unconfined compression of a cylindrical snow sample by a brittle compression rate of $4 \cdot 10^{-2}$ s^{-1}. The initial sample density equals 408 kg/m^3. The temperature is -16 °C and the initial bonding parameters are $N_b = 3.0$ and $\frac{r_b}{r_g} = 0.5$

Fig. 6 Unconfined compression of a cylindrical snow sample by a brittle compression rate of $4 \cdot 10^{-2}\,s^{-1}$. The initial sample density equals 408 kg/m^3. The temperature is $-16°C$ and the initial bonding parameters are $N_b = 3.0$ and $\frac{r_b}{r_g} = 0.5$

(a) $\varepsilon_l = 3.6\%$.   **(b)** $\varepsilon_l = 8.8\%$.   **(c)** $\varepsilon_l = 24.0\%$.
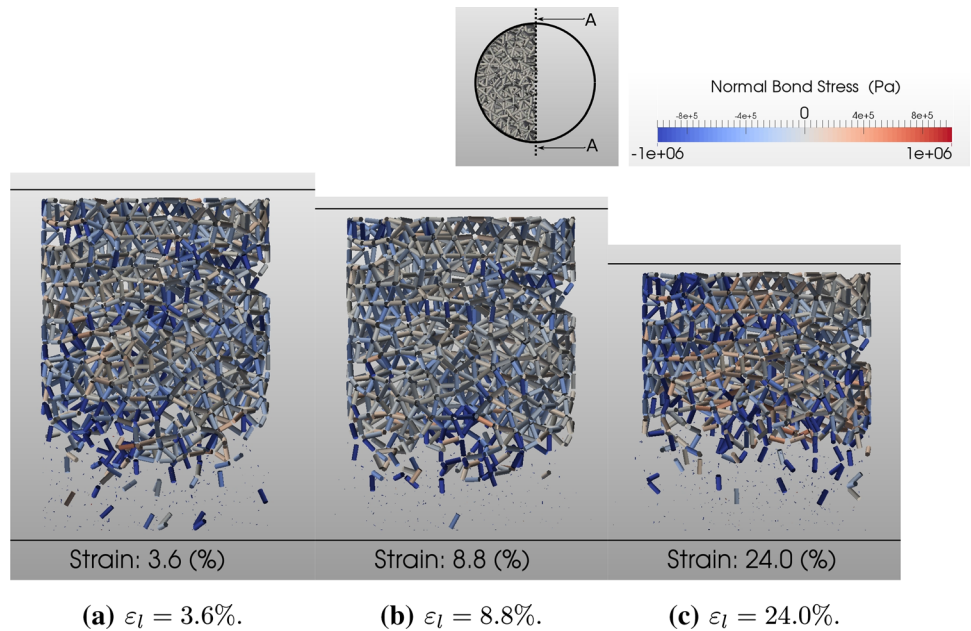
part of the sample leaving the upper part intact to a large extent as shown in Fig. 6 for the bond network. It is worth noting that the model employed in this work does not allow grain breakage. Furthermore, after bond fracture, no debris or additional friction is created.

Figures 5 and 6 show clusters of grains and individual grains detaching from the sample which indicates that bonds hardly experience relaxation under high strain rates. Therefore, any creep that may take place is negligible in the regime considered. A similar but even more amplified performance is recognized for a snow sample of an initial density of $\rho_0 \sim 511$ kg/m^3 that is loaded with a strain rate

of $\dot{\varepsilon} = 4 \cdot 10^{-1}\,s^{-1}$ and is depicted at a strain state of 8.8% in conjunction with particle velocities in Fig. 7.

Under loading conditions applied particles of the upper part of the sample break off that is also visualised by the velocity vectors of respective grains. Fig. 7b shows also that the remaining part of the snow sample is weakly loaded and thus, does almost not carry any load and almost all deformation energy is released by the surface fracture mechanisms.

These findings for the location of rupture correlate nicely with the density distributions shown in Fig. 3. For

Fig. 7 Unconfined compression at 8.8% strain of a cylindrical snow sample by a brittle compression rate of $4 \cdot 10^{-1}\,s^{-1}$. The initial sample density equals 511 kg/m^3. A temperature of $-10°C$ is applied and the initial bonding parameters are $N_b = 3.5$ and $\frac{r_b}{r_g} = 0.5$. The arrows indicate the particle velocity

(a) The snow grains are coloured to allow visual tracking.

(b) The bond structure is coloured by the normal stress component.
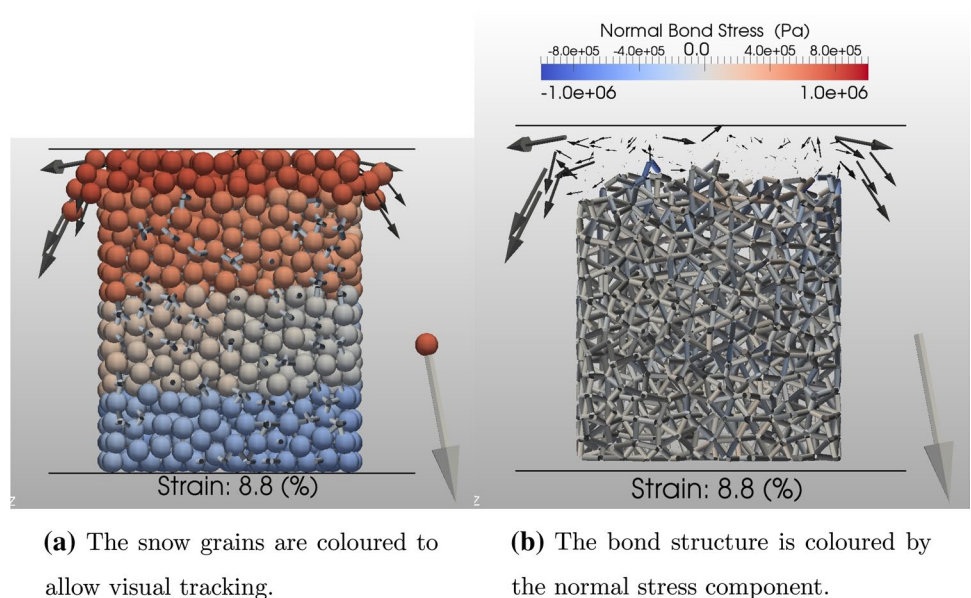
sample 1 and 5 regions of lowest densities are found at the bottom and top part of the sample, respectively, and these are the regions for the onset of brittle failure e.g. fracture as depicted in Figs. 6 and 7. Less grains occupy regions of lower densities so that only a reduced number of bonds may be formed between neighbouring grains resulting in a weaker snow layer compared to the rest of the sample.

3.2.2 Deformation behaviour in the transitional regime

In order to investigate the transitional behavior, a snow sample with an initial density of $\rho_0 = 408$ kg/m^3 was subjected to a strain rate of $\dot{\varepsilon} = 4 \cdot 10^{-4}$ s^{-1}. We conducted several simulation at a different temperature each: $T = -4\,°C$, $T = -10\,°C$ and $T = -16\,°C$. Figure 8 depicts the predicted stress-strain relationship in conjunction with the experimental data of [4].

The stress increases continuously with increasing strain during an initial loading period. Contrary to brittle behavior, the sample does not experience any abrupt rupture

e.g. collapse of stress. Once the yield stress is reached, a strain-softening behavior is observed for the remaining of the loading period. This characteristic manifests itself as an alternating stress versus strain and agrees well with the measurements of [4]. The processes in ductile-to-brittle transition have been studied by [19] from a continuum mechanics perspective.

Figures 9 and 10 show the arrangement of grains bonds of the sample at a temperature of $-10\,°C$ of Fig. 8, respectively, for an axial strain of $\varepsilon_l = 1.6\%$, $\varepsilon_l = 5.2\%$, $\varepsilon_l = 20.8\%$ and $\varepsilon_l = 27.6\%$.

Figure 9a shows the deformed sample during the initial stress build-up at a strain state of $\varepsilon_l = 1.6\%$. At this state the sample contracts uniformly with no change in shape and the bond structure has not experienced any fracture. For smaller strain rates, bond stress and the non-linear stress increase reveal that the bonds have time to grow and relax stress due to creep. The strain states between $\varepsilon_l = 5.2\%$ and $\varepsilon_l = 20.8\%$ may be identified as a period of strain softening derived from Fig. 8, before stress

Fig. 8 Unconfined compression of a cylindrical snow sample of 408 kg/m^3 in the transition regime between ductile and brittle behavior. The purple curves show the predicted results at different temperatures. The black curves depict unconfined compression tests of [4] at transition rates
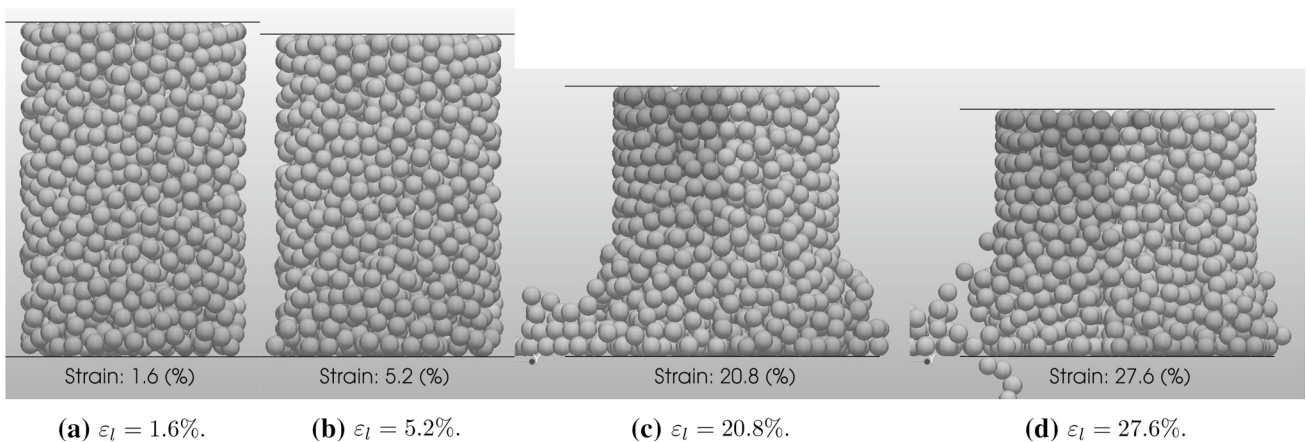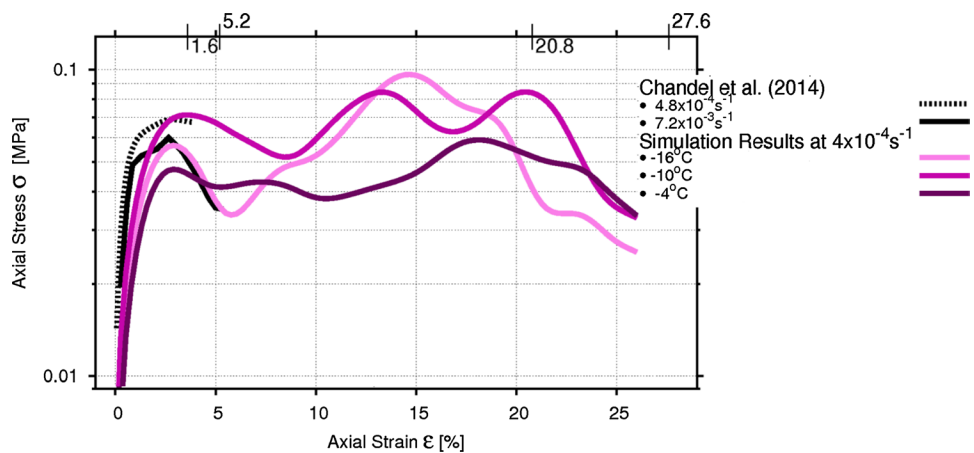

(a) $\varepsilon_l = 1.6\%$.   **(b)** $\varepsilon_l = 5.2\%$.   **(c)** $\varepsilon_l = 20.8\%$.   **(d)** $\varepsilon_l = 27.6\%$.

Fig. 9 Unconfined compression by a transition rate of $4 \cdot 10^{-4}$ s^{-1}. The initial sample density equals 408 kg/m^3. The temperature is $-10°C$ and the bonding parameters are $N_b = 3.5$ and $\frac{r_b}{r_g} = 0.5$
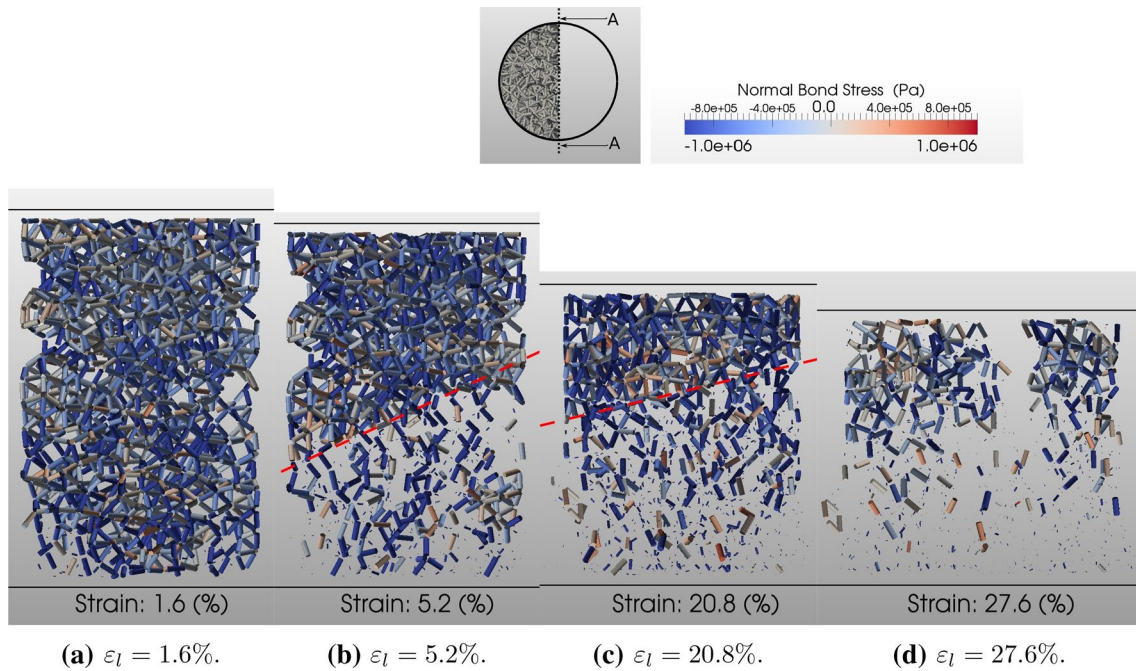
Fig. 10 The bond structure is depicted at increasing strain states and coloured by the normal stress component (− compression / + tension). An unconfined compression rate of $4 \cdot 10^{-4}$ is applied. The initial sample density equals 408 kg/m³. The temperature is − 10°C and the bonding parameters are $N_b = 3.5$ and $\frac{r_b}{r_g} = 0.5$

decreases with increasing strain. Although the shape of the sample in Fig. 9b at a strain state of $\varepsilon_l = 5.2\%$ is still intact, the bond network has disintegrated in the bottom part of the sample to a large extent as shown in Fig. 10b. Higher strain states e.g. $\varepsilon_l = 20.8\%$ and $\varepsilon_l = 27.6\%$ in Figs. 9c and d are associated with large deformations of the cylindrical shape so that clumps of grains break off. These deformations are associated with a further disintegration of the bond network as depicted in Figs. 10b-d whereby more and more failure of bonds occurs mainly below an inclined fracture plane indicated by the red dashed lines in Fig. 10b and c. After each stress build up, a new fracture surface develops due to the rupture of a large number of bonds between the new and the previous fracture surfaces [6]. observed a similar fracture type named type 2 to which he referred to as multiple plane failure.

Bonds in the upper part of the sample above the fracture surface experience further stress due to deformation. The remaining bonds in the damaged part e.g. below the fracture surface are mainly oriented along the loading direction which indicates that rupture of bonds was caused by the shear stress.

At a strain state of $\varepsilon_l = 27.6\%$ in Fig. 9 the sample breaks gradually apart during the final period of strain-softening. The sample becomes more and more fragile due to a decreasing number of bonds, in particular along the direction perpendicular to the loading axis along which major cracks develop.

Concluding any stage of deformation at a transitional strain rate of $\dot{\varepsilon} \sim 4 \cdot 10^{-4}$ s^{-1} intra- and inter-granular creep occurs and determines the macroscopic behavior to a large extent. A lot of bonds relax stress to a certain degree caused by creep. In addition, new bonds developed and growth of existing bonds resist deformation, however, are not always strong enough to prevent local failure of the sample.

3.2.3 Deformation behaviour in the ductile regime

The present model approximated the grain-scale viscoplastic flow law using the secondary creep model from [3]. The secondary creep rate $\dot{\varepsilon}_s$ is considered the minimum creep rate in ice such that $\dot{\varepsilon}_s = min(\dot{\varepsilon}_t) = min(\dot{\varepsilon}_p) < max(\dot{\varepsilon}_t) < max(\dot{\varepsilon}_p)$, $\dot{\varepsilon}_p$ being the primary creep rate and $\dot{\varepsilon}_t$ the tertiary creep rate [21]. Although grain-scale experiments of Szabo and Schneebeli [26] on which the model is calibrated are performed at very short time-scale, the use of steady creep properties from [3] enables the model to be safely employed to simulate compression tests where ductile behavior is exhibited on the macro-scale. Furthermore, the stress level in ice grains is considered to remain small due to grain mobility leading to macro- and meso-scale plastic work being dissipated through breakage of bonds and grain rearrangement. Hence, grain breaking and metamorphism are neglected.

Therefore, a ductile deformation behavior was predicted for a snow sample of $\rho_0 = 408$ kg/m³ with a strain rate of $\dot{\varepsilon} = 4 \cdot 10^{-6}$ s^{-1} at temperature of $T = -4$ °C. In order to

investigate the influence of bonding properties, two numerical samples were employed with the following set of parameters: $N_b = 3.0$, $r_b/r_p = 0.5$ and $N_b = 4.0$, $r_b/r_p = 0.9$. The obtained results are shown in Fig. 11 in conjunction with experimental data of [20, 25] and [4].
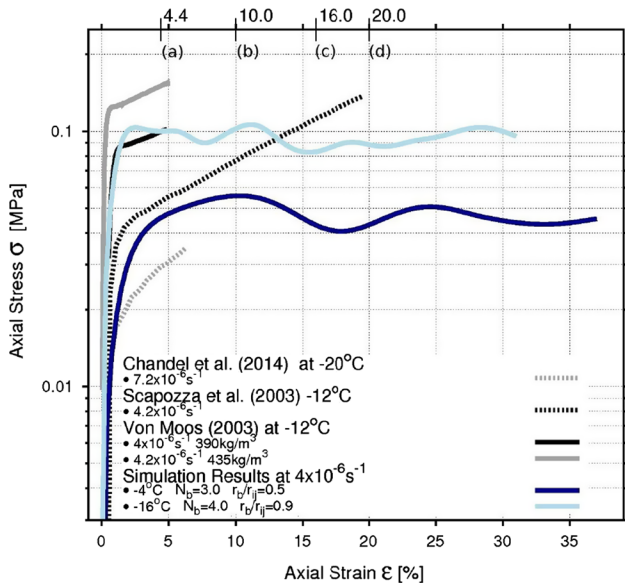

Fig. 11 Unconfined compression of a cylindrical snow sample by ductile rates at different temperatures. The blue curves are the predicted results for a sample of an initial density of 408 kg/m³. The grey and black curves are unconfined compression measurements by [20, 25] and [4] (colour figure online)

The initial stress-strain interrelationship conforms to a high gradient that flattens out after reaching the yield strength σ_y. Hereafter, the yield stress follows a more or less constant level independent of the strain. The initial stiffness of the predicted profiles increases with increasing bonding properties, i.e. N_b and $\frac{r_b}{r_g}$. This agrees well with the observations of [6], who states that the strength and stiffness increase with increasing sintering time [25]. also observed an increase of stiffness but related it to higher densities. A similar trend is observed for the measurements presented in Fig. 11, however, after reaching the yield stress a period of work hardening follows as reported by [6, 20] and [25]. The predicted results miss a work hardening characteristic which is attributed to an over-predicted creep.

Figs. 12 and 13 for the grain structure and the bond network, respectively, represent the sample at an axial strain of $\varepsilon_l = 4.4\%$, $\varepsilon_l = 16.0\%$, $\varepsilon_l = 20.0\%$.

Both shape and bonds of the sample experience hardly any topological changes until the yield stress is reached at a strain of $\varepsilon_l = 4.4\%$ as depicted in Figs. 12a and 13a. At this stage the sample is compacted almost uniformly with no change in shape and bonds experience a moderate stress level. This tendency is observed until a strain state of $\varepsilon_l = 20.0\%$ is reached shown in Figs. 12b and 13b. At this stage the sample deforms in the bottom part that causes an inhomogeneous distribution of stress throughout the bond structure whereby the stress increases towards the bottom of the sample. Also, an increasing number of bonds along
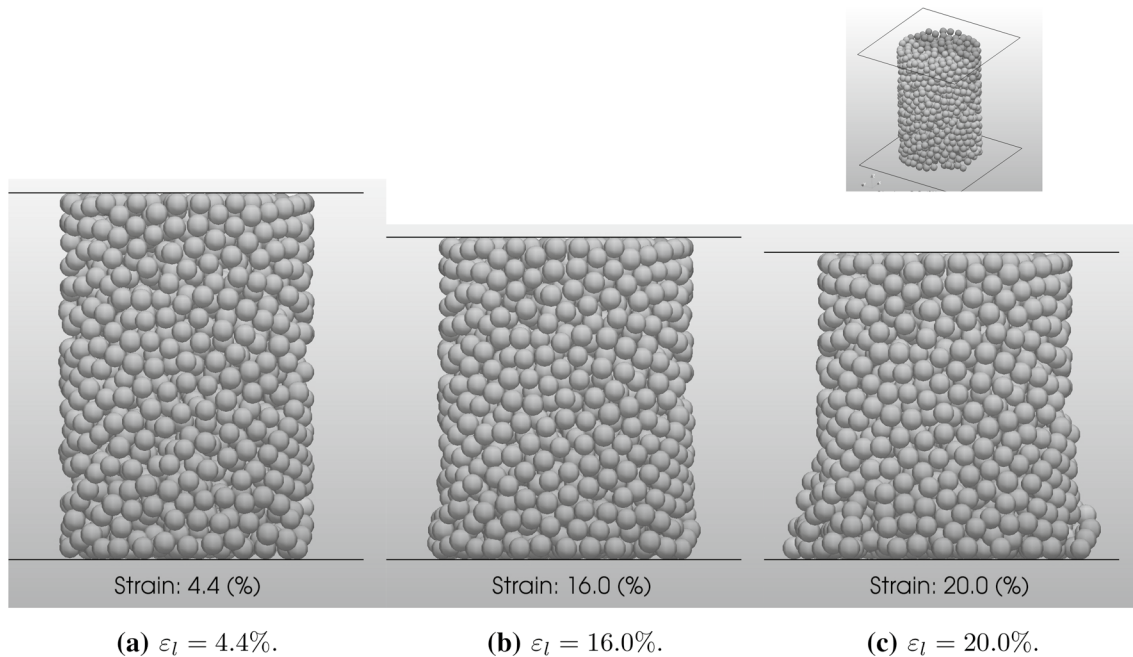

(a) $\varepsilon_l = 4.4\%$.   **(b)** $\varepsilon_l = 16.0\%$.   **(c)** $\varepsilon_l = 20.0\%$.

Fig. 12 Unconfined compression of a cylindrical snow sample for a ductile compression rate of $4 \cdot 10^{-6}$ s⁻¹. The initial sample density equals 408 kg/m³. The temperature is -4 °C and the bonding parameters are $N_b = 3.0$ and $\frac{r_b}{r_g} = 0.5$
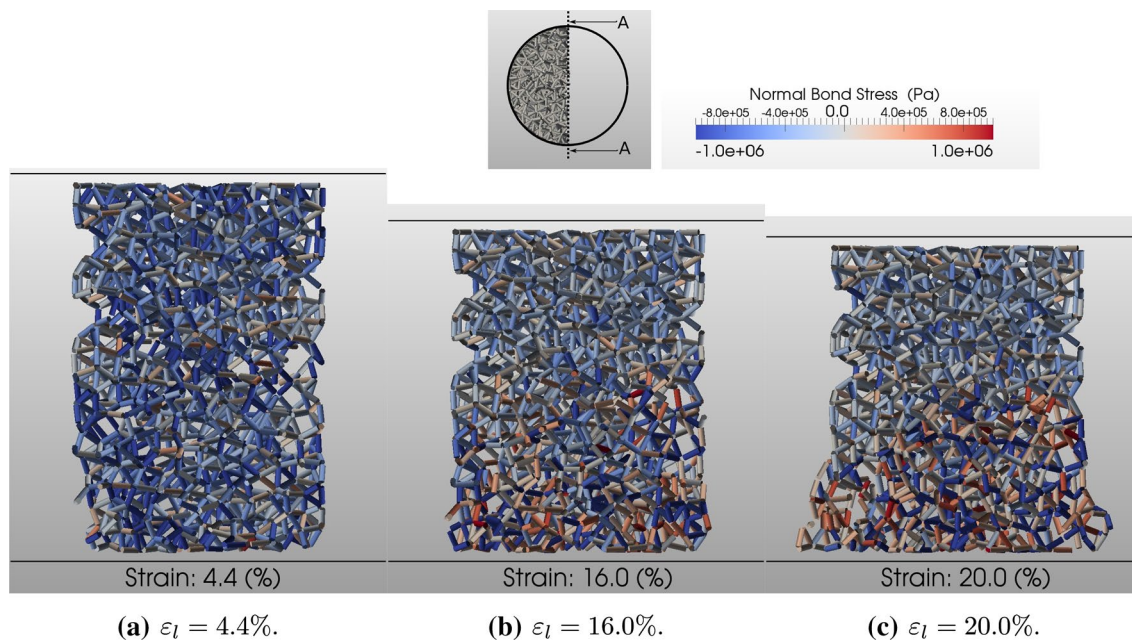
Fig. 13 The bond structure is depicted at increasing strain states and coloured by the normal stress component (− compression / + tension). An unconfined compression rate of $4 \cdot 10^{-4}$ s^{-1} is applied. The initial sample density equals 408 kg/m^3. The temperature is $-10\,^\circ$C and the bonding parameters are $N_b = 3.5$ and $\frac{r_b}{r_g} = 0.5$

a predominant radial direction experiences tension due to the higher radial deformation at the bottom of the sample. However, bonds are able to relax the stress under the low strain rate, and thus, avoid failure due to creep.

3.2.4 Relationship between snow yield strength and strain rate

The previous findings for the brittle, transitional and ductile regime under unconfined compression tests are summarised in the current section as yield strength versus strain rate whereby the yield strength is defined as the maximum stress reached while straining a sample. Yield strength versus strain rate, coloured for the ductile, transitional and brittle regime, is shown in Fig. 14 for predicted results and measurements, respectively.

The unconfined tests under brittle compression rates of [6] at temperature of $T = -13\,^\circ$C analyse the brittle strength dependent on the sintering age of snow, i.e. bonding properties and therefore, are marked with the sintering time before the compression tests began. These results highlight that the sintering period belongs to one of the most influential properties affecting the strength of a snow pack. In addition, these results of [6] are presented to emphasise the impact of snow history on spread in yield stress. Furthermore, Fig. 14 also includes a curve of [6] identifying the ductile to brittle transition rate [6]. showed that the transition rate increases
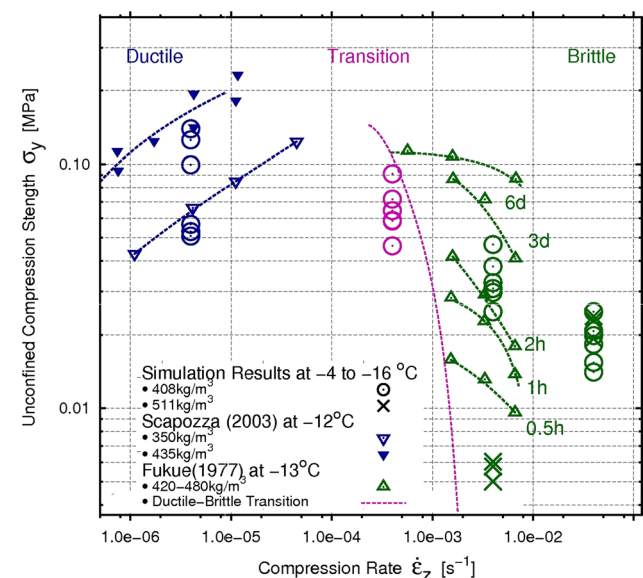

Fig. 14 Unconfined compression strength versus strain rate for snow densities of $\rho = 400$ kg/m^3 to $\rho = 500$ kg/m^3. The lines interpolate the measurements by [6] and [25]

with decreasing sintering time, while [18] observed a decrease with decreasing temperature.

[25] used naturally sintered snow for their investigation for which the increase in density is an indicator for a longer sintering time. Their results are depicted in Fig. 14

at a temperature of $T = -12\,°C$ for densities of $\rho_0 = 350$ kg/m^3 and $\rho_0 = 435$ kg/m^3, respectively, to which the predicted results agree well. However, the predicted results at a strain rate $\dot{\varepsilon} = 4.0 \cdot 10^{-3}$ indicate a deceasing strength with increasing density. It is attributed to the fact that the sample with a higher density has smaller bond radius e.g. weaker bonds that reduce the strength.

Summarising, both measurements and predicted results in Fig. 14 demonstrate a very apparent dependency of snow strength on strain rate. While unconfined compression strength increases with increasing strain rates in the ductile regime, a transitional regime is encountered at maximum values that then migrates into the brittle regime with falling strength versus strain rates. In addition, the transitional regime appears with a further influence of temperature and sintering time as reported by [6, 18 and 25].

3.2.5 Influence of initial bonding on snow strength

Long sintering times i.e. age of snow correspond to stronger bonding properties that were investigated by [6]. He used a sealed container to avoid density changes and to sinter snow for 0.5, 1 and 2 hours and 3 days of which the measurements of strength versus strain rate are depicted in Fig. 15.

Since longer sintering periods affect the bond network it is expressed through coordination number N_b and bonding radius $^{r_b}/\overline{r}_g$ in the current study. For this purpose three bonding configurations presented in table 4 were chosen:

Fig. 15 Unconfined compression strength versus the bonding strength, i.e. sintering age, and strain rate. The black lines interpolate the measurements by [6]. A coloured line indicates a predicted result. The different bonding strengths are indicated by colour and the different sintering ages of snow within the measurements are noted next to the curves (colour figure online)

Table 4 Three selected bonding configurations

$r_b/\overline{r}_g$	0.3	0.5	0.9
N_b	2.5	3.0	4.0

Results of the compression strength were extracted from predictions obtained under brittle strain rates of $\dot{\varepsilon} = 0.4$ s^{-1}, $\dot{\varepsilon} = 4 \cdot 10^{-2}$ s^{-1} and $\dot{\varepsilon} = 4 \cdot 10^{-3}$ s^{-1} and a transition rate of $\dot{\varepsilon} = 4 \cdot 10^{-4}$ s^{-1} are presented with the experimental data in Fig. 15.

Both predicted results and measurements show an increase of the unconfined compression strength with increasing bonding properties i.e. sintering age. Both results further describe an increase in strength with decreasing strain rate which is very uncommon to other brittle material. Although weakened by the logarithmic scale of the ordinate axis, experiments and predictions reveal that the strength increases stronger e.g. larger gradients with reducing strain rate that is also captured well by the developed models. Under these conditions, bonds relax the developed stress as described by the elastic—viscoplastic bond and creep model and is described as a 'healing' process of snow by [30]. Predicted results also indicate that the compression strength obeys an asymptotic behavior with increasing strain rates in the brittle regime. Although the configuration $N_b = 4.0$ is only represented by 2 values, we assume that it follows a similar asymptotic trend and therefore, is not joined by a straight line. The same characteristics were labelled as the second kind of brittle behavior by [18] and confirmed by [30]. Transition from brittle to second kind of brittleness takes place at a rate of $\dot{\varepsilon} \sim 5 \cdot 10^{-2}$ s^{-1} for temperatures of $T = -7\,°C$ to $T = -8\,°C$ according to [18] and is very well predicted. Above this critical rate, the strength does hardly change with increasing rate, temperature and bonding properties. Finally, it has to be noticed that the predictions and the experiments show that below a certain size in bonding properties, i.e. sintering time, the bonding structure of a sample loses its influence on the strength almost entirely.
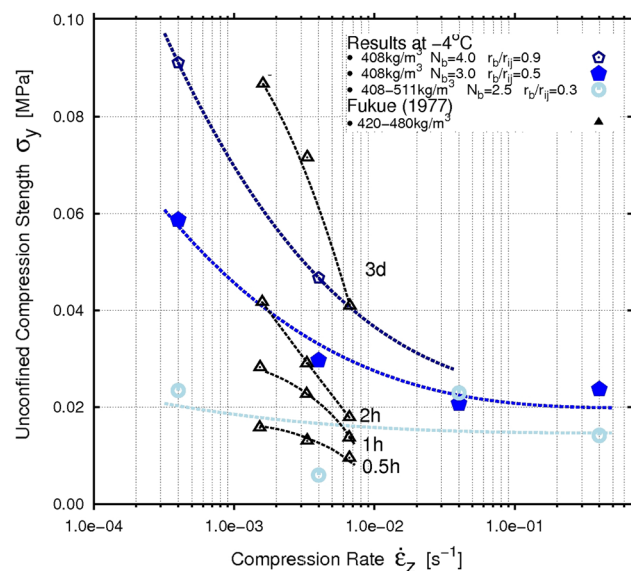
3.3 Confined compression tests of snow

Contrary to the previous sections addressing unconfined compression test, this section describes confined tests, in which the cross-sectional area of the sample remains constant. Therefore, strain state ε_l and averaged density ρ_t of a sample at any time during compression are related as follows:

$$\rho_t = \rho_0 \cdot \left(1 - \varepsilon_l\right)^{-1} \tag{19}$$

where ρ_0 is the initial density of the sample and has a dominant influence on a compression test.

3.3.1 Initial Density Dependency of Stress

[1] conducted confined compression tests with isothermally sintered snow under brittle strain rates of $\dot{\varepsilon} = 4 - 16 \mathrm{s}^{-1}$ at temperatures of $T = -1\,°C$, $T = -4\,°C$, $T = -10\,°C$ and $T = -32\,°C$ for varying initial densities. His measurements for a temperature of $T = -4\,°C$ in conjunction with predicted results under strain rates of $\dot{\varepsilon} = 0.4 - 4\,\mathrm{s}^{-1}$ for initial densities of $\rho_0 =$ 408 kg/m^3, $\rho_0 =$ 511 kg/m^3 and $\rho_0 =$ 578 kg/m^3 are depicted in Fig. 16 whereas Fig. 17 shows respective results for temperatures below $T < -10\,°C$.

For temperature range examined the predicted results agree well with experimental data illustrating that the strength at any fixed strain state increases significantly with increasing initial density. The profiles for initial densities of $\rho_0 = 578\,$kg/m^3 and $\rho_0 = 511\,$kg/m^3 in Figs. 16 and 17 reveal a continuous stress increase with increasing strain. However, the gradient becomes smaller once the point of yield stress has been passed.

A different behavior is observed for an initial density of $\rho_0 = 408\,$kg/m^3 in Figs. 16 and 17. Snow sample responds during the first part of compression with a sawtooth-like shape that is a well-known phenomenon of the brittle regime. Stress build-up and release alternate that is caused by continuously fracturing bonds through the snow sample with increasing strain. Each subsequent stress build-up reaches a higher strength than its predecessor. After a sufficiently large compression of the sample the stress follows a continuous profile versus strain. This behavior was also monitored by [6]. He projected the continuous part of the curve backward on the strain axis and extracted the threshold density at which the sawtooth shape of the lower initial density curve increases
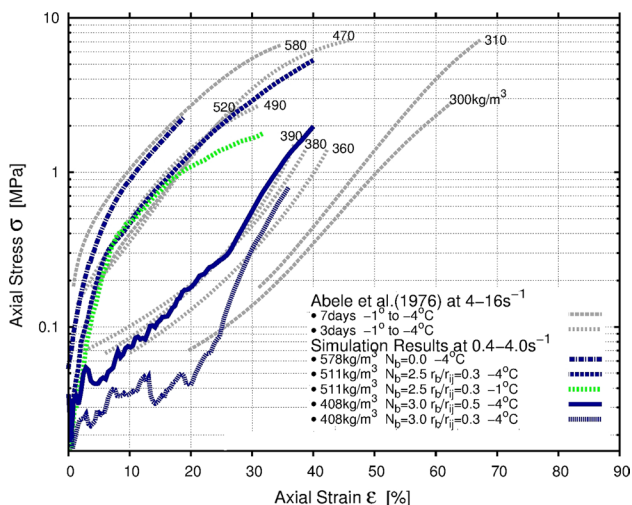

Fig. 16 Confined compression of a cylindrical snow sample at $T = -4\,°C$ and various initial densities loaded with high rates of strain $\dot{\varepsilon} = 0.4 - 4\,\mathrm{s}^{-1}$. The grey curves are confined compression measurements by [1] (colour figure online)

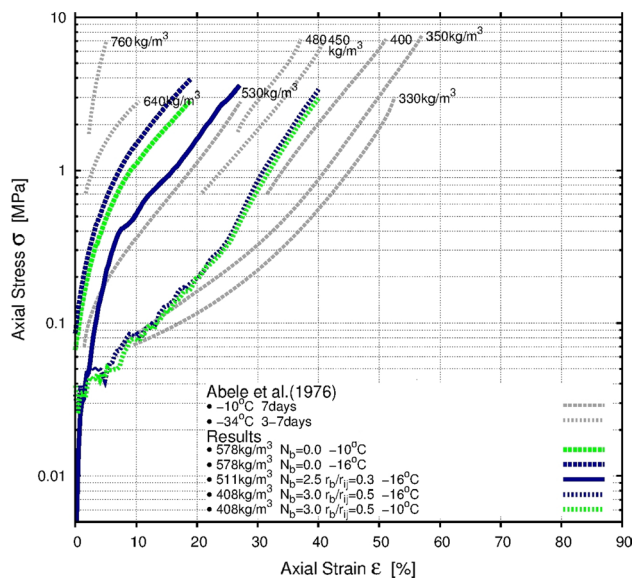**Fig. 17** Confined compression of a cylindrical snow sample at $T \leq -10\,°C$ and various initial densities loaded with high rates of $\dot{\varepsilon} = 0.4 - 4\,\mathrm{s}^{-1}$. The grey curves are confined compression experiments by [1]

continuously. Thus, he assessed threshold densities between $\rho = 420 - 460\,$kg/m^3 at a strain rate of $\dot{\varepsilon} = 4\,\mathrm{s}^{-1}$. A predicted threshold density of $\rho = 450\,$kg/m^3 in Figs. 16 and 17 falls well into the experimentally determined interval and proofs the predictive capabilities of the models developed. [1] also reported the threshold effect for samples with initial densities between $\rho_0 = 300\,$kg/m^3 and $\rho_0 = 400\,$kg/m^3. They observed a change in curvature for a current density between $\rho = 400$ kg/m^3 and $\rho = 500\,$kg/m^3 at strains from $\varepsilon = 20\%$ to $\varepsilon = 40\%$ which is well matched by the predictions in Figs. 16 and 17.

3.3.2 Temperature dependency of stress

The temperature dependency of stress is largely determined by creep on a micro-scale for confined compression tests in the brittle regime. In general, snow becomes softer and more viscous with higher temperature. [1] showed that the brittle compression behavior can be separated into two regions at a temperature of $T \sim -10\,°C$ shown in Figs. 16 and 17. Fig. 16 shows a continuous decrease of the gradient with increasing strain at temperatures $T > -10\,°C$ for both experiments and predictions, while the gradients in Fig. 17 remain constant to a large extent for temperatures $T < -10\,°C$ at large strains.

4 Conclusion

In this study the advanced micro-mechanical approach, developed in Part I of this article, was employed to predict brittle and ductile deformation behavior of snow including

its transitional regime on both a micro- and macro-scale. On a microscopic scale, bonds experience tension, compression, bending and torsion during deformation. Bond growth, compressive response and fracture of bonds were successfully validated through experimental data. This modelling framework was applied to predict snow behavior on a macroscopic scale for confined and unconfined compression tests of snow of which the results obtained were compared to large sets of experimental data.

The strain-stress interrelationship was well predicted in both the brittle and ductile regime separated by a strain rate of $\dot{\varepsilon} = 4 \cdot 10^{-3}\,\mathrm{s}^{-1}$ by a single numerical approach, although the ductile behavior lacks the work-hardening effect under unconfined compression conditions. In addition the dependency of stress on initial density and temperature of a snow sample was captured very well. A good performance was achieved for describing the effect of sintering i.e. snow history and was proven to be the most influential parameter on snow strength. However, results shown in this study might be size-dependent therefore, the model parameters should not be extrapolated beyond the specimen size presented herein. Future efforts will focus on work-hardening under ductile conditions during unconfined compression tests.

Compliance with ethical standards

Conflict of interest The authors declare that they have no known competing financial interests or personal relationships that could have appeared to influence the work reported in this paper.

References

1. Abele, G., Gow, A.: Compressibility characteristics of compacted snow. Technical Report. U.S. Cold Regions Research and Engineering Laboratory (1976)
2. Akkok, M., Ettles, C.M.M., Calabrese, S.J.: Parameters Affecting the Kinetic Friction of Ice. Journal of Tribology **109**, 552–559 (1987). https://asmedigitalcollection.asme.org/tribology/article-pdf/109/3/552/5696634/552_1.pdf
3. Barnes, P., Tabor, D., Walker, J.C.F., F.R.S.: The friction and creep of polycrystalline ice. In: Proceedings of the Royal Society of London. Series A, Mathematical and Physical Sciences Proc. Roy. Soc. Lond. A, pp. 127–155
4. Chandel, C., Srivastava, P.K., Mahajan, P.: Micromechanical analysis of deformation of snow using X-ray tomography. Cold Reg. Sci. Technol. **101**, 14–23 (2014)
5. Chiaia, B., Cornetti, P., Frigo, B.: Triggering of dry snow slab avalanches: stress versus fracture mechanical approach. Cold Reg. Sci. Technol. **53**, 170–178 (2008)
6. Fukue, M.: Mechanical performance of snow under loading. Tokai University Press, Tomigaya (1979)
7. Gammon, P.H., Kiefte, H., Clouter, M.J., Denner, W.W.: Elastic constants of artificial and natural ice samples by brillouin spectroscopy. J Glaciol **29**, 433–460 (1983)
8. Gaume, J., Chambon, G., Eckert, N., Naaim, M.: Influence of weak-layer heterogeneity on snow slab avalanche release: application to the evaluation of avalanche release depths. J Glaciol **59**, 423–437 (2013)
9. Gaume, J., Chambon, G., Reiweger, I., Herwijnen, A.V., Schweizer, J.: On the failure criterion of weak-snow layers using the discrete element method. In: Proceedings International Snow Science Workshop (ISSW 2014),Banff, Alberta, Canada, 681–688, (2014)
10. Gaume, J., Schweizer, J., van Herwijnen, A., Chambon, G., Reuter, B., Eckert, N., Naaim, M.: Evaluation of slope stability with respect to snowpack spatial variability. J. Geophys. Res. Earth Surf. **119**, 1783–1799 (2014. https://agupubs.onlinelibrary.wiley.com/doi/pdf/10.1002/2014JF003193
11. Gaume, J., Van Herwijnen, A., Chambon, G., Birkeland, K.W., Schweizer, J.: Modeling of crack propagation in weak snowpack layers using the discrete element method. Cryosphere **9**, 1915–1932 (2015)
12. Hagenmuller, P., Chambon, G., Naaim, M.: Microstructure-based modeling of snow mechanics: a discrete element approach. Cryosphere **9**, 1969–1982 (2015)
13. Heierli, J., Gumbsch, P., Zaiser, M.: Anticrack nucleation as triggering mechanism for snow slab avalanches. Science **321**, 240–243 (2008). https://science.sciencemag.org/content/321/5886/240.full.pdf
14. Hertz, H.: 1881 Über die Berührung fester elastischer Körper. Journal für die reine und angewandte Mathematik **92**, 156–171 (1881)
15. Kabore, B., Peters, B., Willibald, C., Thiele, T., Schneebeli, M.: Multi-scale modelling of snow mechanics. In: 41st Solid Mechanics Conference (SOLMECH 2018), Warsaw, Poland (2018)
16. Kabore, B.W., Peters, B.: Micromechanical model for sintering and damage in viscoelastic porous ice and snow. Part I: Model and calibration. Int. J. Solids Struct. 185-186, 324–333 (2020a). arXiv:1808.04394
17. Kabore, B.W., Peters, B.: Micromechanical model for sintering and damage in viscoelastic porous ice and snow. part ii: Validation. Int. J. Solids Struct. **185–186**, 281–291 (2020b)
18. Kinosita, S.: Compression of snow at constant speed. In: International Conference on Low Temperature Science: Physics of Snow and Ice. pp. 911–927 (1967)
19. Löwe, H., Zaiser, M., Mösinger, S., Schleef, S.: Snow mechanics near the ductile-brittle transition: Compressive stick-slip and snow microquakes. Geophysical Research Letters **47**, e2019GL085491. E2019GL085491 https://doi.org/10.1029/2019GL085491 (2020). https://agupubs.onlinelibrary.wiley.com/doi/pdf/10.1029/2019GL085491
20. von Moos, M.: Untersuchungen "uber das visko-elastische verhalten von Schnee auf der Grundlage von triaxialen Kriechversuchen. Ph.D. thesis. ETH Z"urich (2001)
21. Morland, L.W.: Primary, secondary and tertiary creep of ice modelled as a viscoelastic fluid. J. Glaciol., **55**, 170–178 (2009)
22. Narita, H.: An experimental study on tensile fracture of snow. Contributions from the Institute of Low Temperature Science, **A32**, 1–37 (1984)
23. Peters, B., Willibald, C., Thiele, T.: SnowDEM meeting 2 - Luxembourg, July 2017, 1–3 (2017)
24. Rycroft, C.H.: Multiscale modeling in granular flow. PhD (2007)
25. Scapozza, C., Bartelt, P.: Triaxial tests on snow at low strain rate. Part II. Constitutive behaviour. J. Glaciol. **49**, 91–101 (2003)

26. Szabo, D., Schneebeli, M.: Subsecond sintering of ice. Appl. Phys. Lett. **90**, 151916 (2007)
27. Varrette, S., Bouvry, P., Cartiaux, H., Georgatos, F.: Management of an academic hpc cluster: The ul experience. In: 2014 International Conference on High Performance Computing Simulation (HPCS), pp. 959–967 (2014)
28. Von Moos, M., Bartelt, P., Zweidler, A., Bleiker, E.: Triaxial tests on snow at low strain rate. Part I. Experimental device. J. Glaciol. **49**, 81–90 (2003)
29. Yong, R., Fukue, M.: Performance of snow in confined compression. J. Terramech. **14**, 59–82 (1977)
30. Yong, R.N., Metaxas, I.: Influence of age-hardening and strain-rate on confined compression and shear behaviour of snow. J. Terramech. **22**, 37–49 (1985)